Article

Suppressed thermal transport in silicon nanoribbons by inhomogeneous strain

Lin Yang[1,9]✉, Shengying Yue[2,9], Yi Tao[3], Shuo Qiao[1], Hang Li[4], Zhaohe Dai[4], Bai Song[1,5], Yunfei Chen[3], Jinlong Du[6]✉, Deyu Li[7] & Peng Gao[6,8]✉

Nanoscale structures can produce extreme strain that enables unprecedented material properties, such as tailored electronic bandgap[1–5], elevated superconducting temperature[6,7] and enhanced electrocatalytic activity[8,9]. While uniform strains are known to elicit limited effects on heat flow[10–15], the impact of inhomogeneous strains has remained elusive owing to the coexistence of interfaces[16–20] and defects[21–23]. Here we address this gap by introducing inhomogeneous strain through bending individual silicon nanoribbons on a custom-fabricated microdevice and measuring its effect on thermal transport while characterizing the strain-dependent vibrational spectra with sub-nanometre resolution. Our results show that a strain gradient of 0.112% per nanometre could lead to a drastic thermal conductivity reduction of 34 ± 5%, in clear contrast to the nearly constant values measured under uniform strains[10,12,14,15]. We further map the local lattice vibrational spectra using electron energy-loss spectroscopy, which reveals phonon peak shifts of several millielectron-volts along the strain gradient. This unique phonon spectra broadening effect intensifies phonon scattering and substantially impedes thermal transport, as evidenced by first-principles calculations. Our work uncovers a crucial piece of the long-standing puzzle of lattice dynamics under inhomogeneous strain, which is absent under uniform strain and eludes conventional understanding.

There is a mantra in the realm of material mechanics, 'smaller is stronger', the science of which took root in the 1950s and is vigorously developing today[6]. As nanomaterials are mechanically much stronger, significantly higher strains can be applied to tune their physicochemical properties than are possible with traditional materials[6,24]. Based on this, we can rationally engineer a spectrum of advanced functionalities ranging from transistors[1,2], solar cells[3] and photodetectors[4] to batteries[5], superconductors[7] and electrocatalysts[8,9]. Despite extensive investigations into strain-engineered electronic properties[1–9], the intricate phonon transport mechanism subjected to inhomogeneous strain remains largely unexplored[17,18]. This is especially frustrating given that precise thermal management stands as a critical bottleneck to device efficiency and lifespan[25,26].

One prevalent method for introducing strain involves growing thin epitaxial layers on substrates with lattice mismatch[1–5,7], such as Si on SiGe (ref. 27), and research has been conducted to investigate thermal transport through various epitaxial layers[16–20,28]. However, although low thermal conductivity (κ) values—even below those of their alloy counterparts—have been observed[16,29], the effects of strain gradient through the epitaxial layers are experimentally difficult to decouple from the interfacial phonon boundary scattering effects[18],

which presents a daunting challenge to drawing a solid conclusion on the physical origin of the ultra-low κ. Similarly, although dislocations and vacancies could scatter phonons in various functional devices[8,9], it remains a formidable challenge to isolate their effects from those of long-range strain fields introduced by these defects, which could also impede thermal transport via an increase in vibrational anharmonicity[21–23]. Consequently, questions regarding the cause of the unusual and somewhat perplexing thermal behaviour in these functional materials have lingered unanswered.

While elastic strain engineering often relies on highly inhomogeneous stress produced by nanoscale deformation (for example, by epitaxial layer growth[1–5], defects and vacancies[8,9], or lithography patterning[30]), most studies of strain effects on thermal transport to date have centred around materials under the simplified condition of uniform stress[10–15]. The major challenges in experimentally quantifying the effects of inhomogeneous strain on thermal transport include applying stress exclusively, without introducing confounding factors (such as interfaces and defects) and combining thermal measurements with sub-nanometre resolved characterization of the phonon spectra. Here, we induce inhomogeneous strain through bending individual silicon nanoribbons (SiNRs) on a custom-fabricated microdevice and measure its effect on

[1]Department of Advanced Manufacturing and Robotics, College of Engineering, Peking University, Beijing, People's Republic of China. [2]Laboratory for Multiscale Mechanics and Medical Science, State Key Laboratory for Strength and Vibration of Mechanical Structures, School of Aerospace, Xi'an Jiaotong University, Xi'an, People's Republic of China. [3]School of Mechanical Engineering and Jiangsu Key Laboratory for Design and Manufacture of Micro-Nano Biomedical Instruments, Southeast University, Nanjing, People's Republic of China. [4]Department of Mechanics and Engineering Science, College of Engineering, Peking University, Beijing, People's Republic of China. [5]Department of Energy and Resources Engineering, College of Engineering, Peking University, Beijing, People's Republic of China. [6]Electron Microscopy Laboratory, School of Physics, Peking University, Beijing, People's Republic of China. [7]Department of Mechanical Engineering, Vanderbilt University, Nashville, TN, USA. [8]International Center for Quantum Materials, School of Physics, Peking University, Beijing, People's Republic of China. [9]These authors contributed equally: Lin Yang, Shengying Yue. ✉e-mail: linyangpku@pku.edu.cn; jldu@pku.edu.cn; pgao@pku.edu.cn
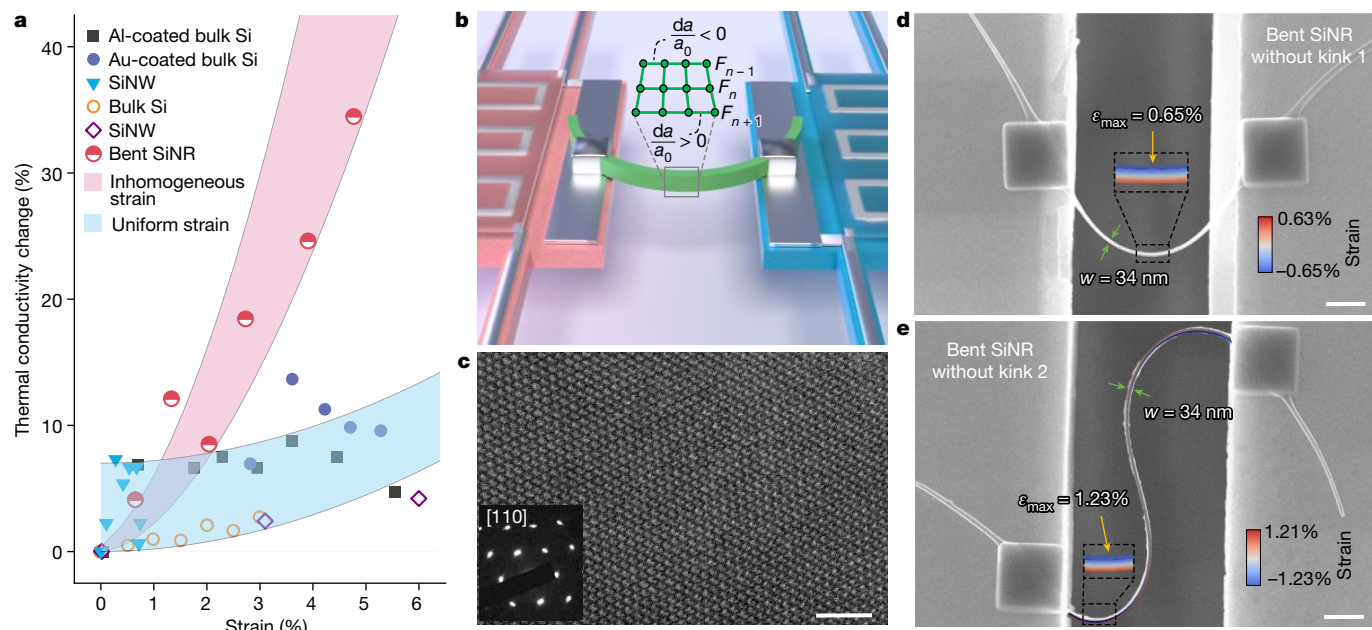
Fig. 1 | Remarkable suppression of thermal transport by inhomogeneous strain in Si. a, κ change as a function of uniform and inhomogeneous elastic strain up to approximately 6%. Both the experimentally measured (filled symbols) and theoretically modelled (empty symbols) κ change for bulk Si (refs. 13,14) and Si nanowire[12,15] under uniform strain remain nearly constant, while the measured data for bent Si nanoribbons rises sharply with increasing strain (half-filled). Note that the larger κ change of several data points under uniform strain of less than 1% is probably due to the measurement uncertainties[14,15]. **b**, Schematic of the suspended micro-bridge device with a bent Si nanoribbon placed to bridge the gap, where the zoomed-in view highlights the distorted lattice due to the inhomogeneous strain. **c**, High-resolution transmission electron microscopy image showing the lattice of a bent Si nanoribbon, where the inset shows a selected area electron diffraction pattern taken along the [110] zone axis. **d,e**, SEM images of two bent Si nanoribbons without kink under the maximum strain of 0.65% (**d**) and 1.23% (**e**). The calculated strain contour is overlaid on top of the SEM images to visualize the strain distribution. Scale bars, 2 nm (**c**), 500 nm (**d,e**).

thermal transport while characterizing the local vibrational spectra using electron energy-loss spectroscopy (EELS) in a scanning transmission electron microscope (STEM) with sub-nanometre resolution. Our results show that a strain gradient of 0.112% per nanometre could lead to a drastic κ reduction of 34 ± 5%, which is over 3-fold of previously demonstrated κ modulation under uniform strain (see summary in Fig. 1a). Taking advantage of recent progress in EELS equipped with a monochromator in an aberration-corrected STEM[31–35], we directly measured the local phonon modes and correlated them with the nanometre-scale strain gradient. Results show that the bending-induced lattice strain gradient significantly alters the vibrational states and broadens the phonon spectra. Coupled with ab initio theoretical modelling, this broadening effect is shown to enhance phonon scattering and shorten phonon lifetimes, ultimately contributing to a suppressed κ.

κ reduction in bent SiNRs

We studied the impact of inhomogeneous strain on phonon transport by bending individual SiNRs on a custom microdevice and measuring κ across a wide temperature range (Fig. 1b). We fabricated single crystalline straight and kinked SiNRs with the same rectangular cross-sectional dimensions (34 nm × 85 nm) using electron-beam lithography, as described in our previous reports (Methods)[36,37]. Using an in-house-built microprobe, we precisely bent the nanoribbon to bridge the gap of the suspended microheater device, with both ends anchored to underlying Pt electrodes using electron-beam-induced deposition of Pt/C (Fig. 1b). This approach introduces inhomogeneous strain without involving complexity from other factors, for example, from interfaces and defects (Extended Data Figs. 1 and 2). As shown in Fig. 1b, atoms below the centre line experience an increase in the interatomic distance a along the axial direction due to tensile strain, while atoms in the upper part experience a reduction in a due to compression. The κ of each sample was then measured using the well-established microthermal bridge scheme (Methods)[38–40]. The high-resolution transmission electron microscopy micrograph of a bent nanoribbon and the selected area electron diffraction pattern verify the single crystalline nature (Fig. 1c and Extended Data Figs. 1 and 2). In Fig. 1d,e, we show the calculated strain distribution for each bent SiNR using finite element analysis (Methods). The maximum principal strain, ε_{max}, for each case is marked near the bending apex. Notably, we ensured that the maximum strain exerted on the SiNRs was low enough to avoid any phase transitions[10]. We also analysed the length of strained SiNRs in which the principal strain on the cross-section was greater than $0.5\varepsilon_{max}$ and found that ratio of the strained portion to the measured total length is roughly the same within two groups of SiNRs without and with kink (Methods).

We compared the κ of stress-free SiNRs (Extended Data Fig. 3) with that of bent SiNRs to understand the impact of inhomogeneous strain on phonon transport. Figure 2a,b shows that the κ of the bent SiNRs is appreciably lower than that of the stress-free SiNR, and the reduction in κ increases as ε_{max} increases. Specifically, the measured κ reduction is 4.2% at 300 K for bent SiNR no. 1 with ε_{max} = 0.65%, which increases to 13.1% for bent SiNR no. 2 with ε_{max} = 1.23%. Note that as the radius of curvature (greater than 1,380 nm) is much larger than the cross-section (34 nm × 85 nm) tested in this work, the curved geometry of the bent SiNRs has only a marginal impact on phonon transport (less than a 3.3% κ reduction, Supplementary Fig. 4)[41]. Thus, the observed κ reduction could be safely attributed to the curvature-induced strain gradient in the bent SiNRs.

To increase the strain gradient and boost the strain effects on phonon transport, bent SiNRs with kink are prepared and measured. The presence of a kink can reduce the length over which the SiNR is deformed, thereby facilitating the development of large strains given similar levels of deflection. Indeed, as shown in Fig. 2c–f, in contrast to the bent SiNRs without kink, the kinked morphology could lead to enhanced ε_{max} as
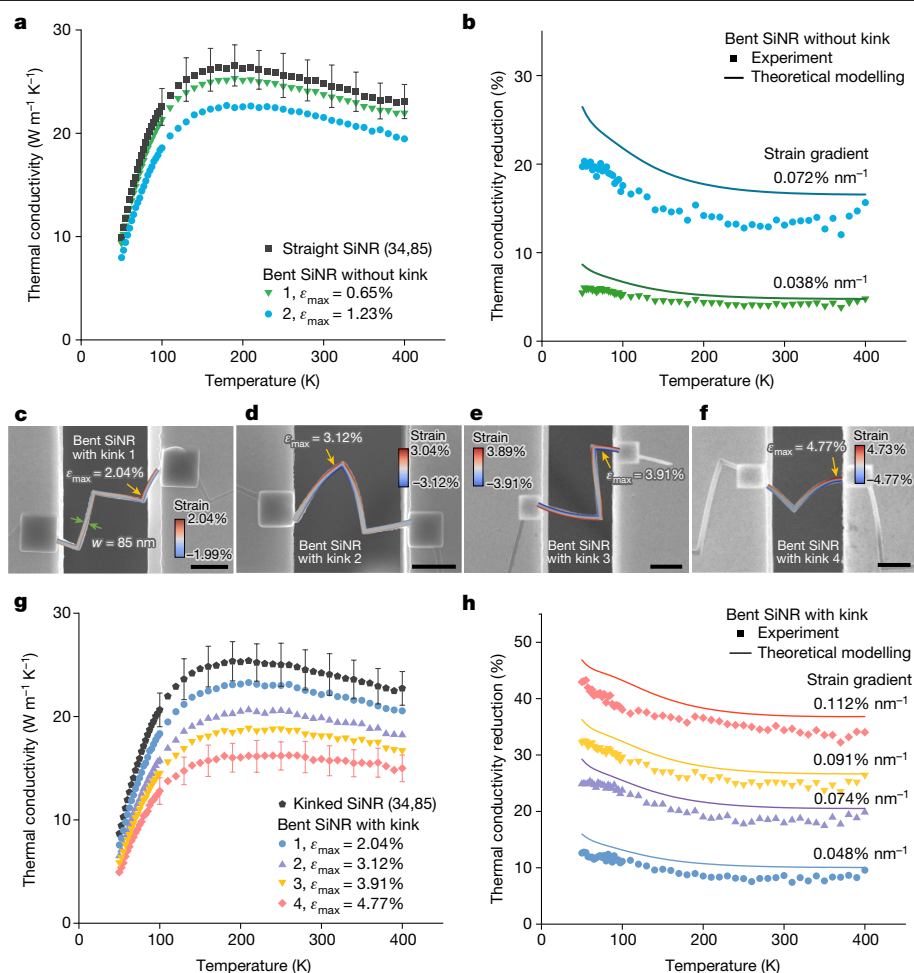
Fig. 2 | Temperature-dependent κ of bent Si nanoribbons. a, Measured κ of bent SiNRs without kink, where the measured results for the stress-free counterpart are also plotted for comparison. **b**, κ reduction of the two bent SiNRs in **a** with respect to the stress-free counterpart. The solid lines are modelled results considering strain gradient-induced phonon scattering. **c**–**f**, SEM images of four bent SiNRs with kink under maximum strain of 2.04% (**c**), 3.12% (**d**), 3.91% (**e**) and 4.77% (**f**). The calculated strain contour is overlaid on top of

the SEM images to visualize the strain distribution. **g**, Measured κ of the stress-free and bent SiNRs with kinks. **h**, κ reduction of four bent ribbons with kink in **g**, compared to the stress-free counterpart, where the solid lines are modelled results. The error bars in **a** and **g** represent uncertainties from measurements of the thermal conductance, length and cross-sectional area of the nanoribbons (Supplementary Note 2). Scale bars, 1 µm (**c**,**d**,**e**,**f**).

evidenced by the finite element analysis results (overlaid on the scanning electron microscope (SEM) images). As a result, the measured κ exhibits a much stronger reduction compared with the stress-free kinked counterpart (Extended Data Fig. 3), and for the bent SiNR with kink no. 4 under ε_{max} of 4.77%, its κ reduction escalates to 34 ± 5% at 300 K, which further increases to 43 ± 6% as the temperature drops to 50 K (Fig. 2g,h). In stark contrast to the previously measured, nearly constant κ of Si under uniform strain[14] up to approximately 5.5%, the bending-induced inhomogeneous strain leads to a steep increasing trend in κ reduction, showcasing the remarkable suppression of thermal transport under a moderate strain gradient of 0.112% per nanometre. Note that this level of strain gradient is several orders of magnitude lower than naturally occurring defects-induced strain gradients[42].

Phonon spectra along strain gradient

To reveal the strain effect on phonon transport, direct measurement of the local phonon spectra of bent SiNRs and characterization of the strain-dependent evolution of phonon modes along the strain gradient are highly desirable. Although the shift in phonon frequency under uniform strain has been observed using conventional techniques, such as Raman spectroscopy[15], the impact of inhomogeneous strain has not

drawn much attention, owing to the substantial experimental challenges associated with resolving the millielectron-volt-scale peak shift at nanometre level. Recent developments in STEM-EELS with combined millielectron-volt (meV) energy resolution and sub-nanometre spatial resolution have enabled nanoscale and atomic-scale probing of lattice vibrational modes in Si (refs. 31,32) and around the structural defects[33]. The experimental setup is illustrated in Fig. 3a, where a 60 keV electron beam is focused to a sub-nanometre spot using aberration correction, and a monochromator is also used to refine its energy resolution[34,35]. An EELS aperture is placed on the diffraction plane to select the scattered electrons with particular momentum transfers to analyse their energy loss, from which the corresponding phonon spectra can be extracted. Figure 3b is a high-angle annular dark field (HAADF) image of a bent SiNR with a kink, overlaid with the calculated strain field. Figure 3c is a zoomed-in view of the bent SiNR, and EELS spectra are recorded at selected points along the strain gradient.

Figure 3d displays the local vibrational spectra for the transverse acoustic and transverse optical modes acquired at five positions (P1 to P5) under different strain states. Notably, the transverse acoustic mode exhibits a blueshift as it transitions from compressive to tensile strain, resulting in a phonon peak shift of approximately 2.2 meV under approximately 6.4% strain difference. Conversely, the transverse optical
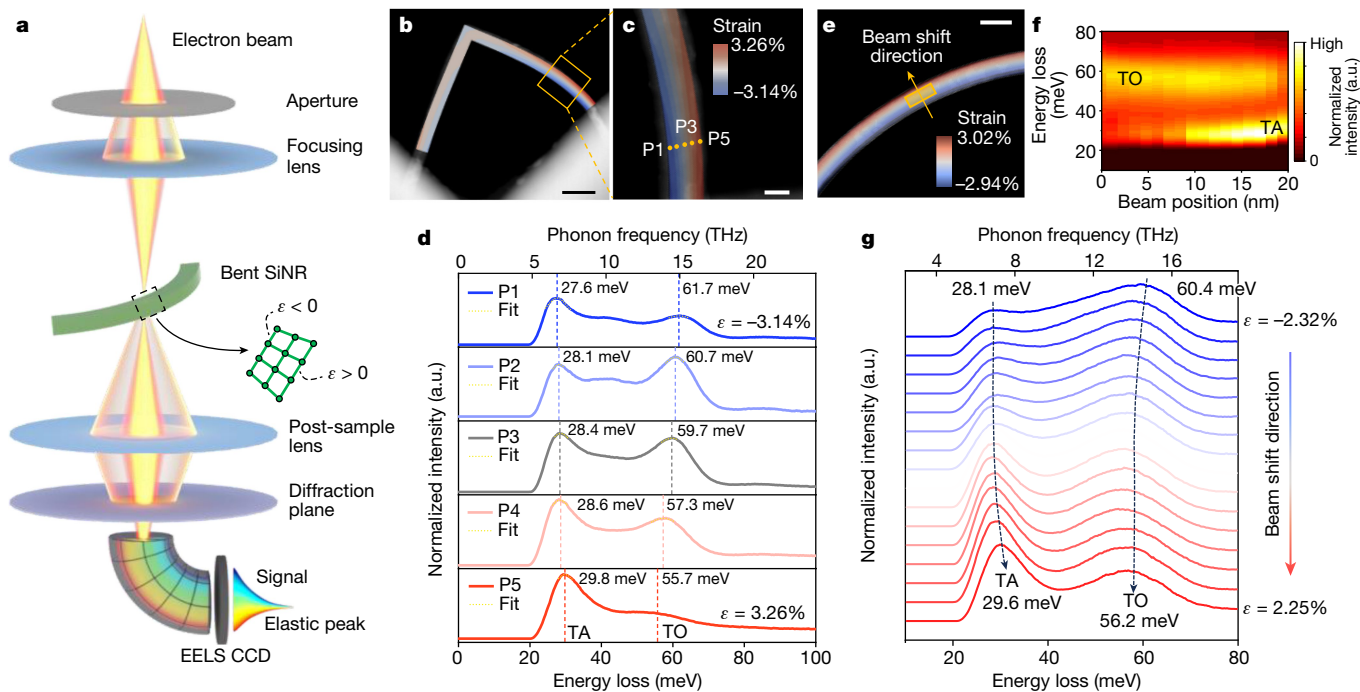
Fig. 3 | Spatially resolving the strain-modulated phonon modes. a, Schematic diagram of STEM-EELS to probe vibrational modes along the strain gradient of a bent Si nanoribbon. **b,c**, An HAADF image of a bent Si nanoribbon with kink (**b**) and zoomed-in view of the region for EELS measurements (**c**), where the calculated strain contour is overlaid on top. **d**, Measured EELS profiles for the transverse acoustic (TA) and transverse optical (TO) phonon modes at different positions (P1 to P5) along the strain gradient, where the transverse acoustic mode exhibits a blueshift of approximately 2.2 meV, whereas the transverse optical mode shows a redshift of approximately 6.0 meV as the elastic strain varies from −3.14% to 3.26%. The peak position is extracted via Gaussian fitting. **e**, An HAADF image for a bent SiNR without kink. The yellow rectangle represents the area where the EELS signals are acquired by summing each column spectra of the three-dimension dataset along the axial direction (perpendicular to the strain gradient) to enhance the signal-to-noise ratio. **f**, Vibrational spectra map for the transverse acoustic and transverse optical modes along the beam shift direction. **g**, Measured EELS line profiles along the strain gradient for the region marked in **e**. Top *x* axis in (**d**) and (**g**) represent the phonon frequency in THz. Scale bars, 200 nm (**b**), 50 nm (**c**, **e**). a.u., arbitrary units.

mode displays a redshift of approximately 6.0 meV as it undergoes the same strain gradient from compressive to tensile strain. To further elucidate the bending-induced phonon frequency shift in SiNRs, the EELS spectra are recorded within the selected rectangular region for another bent SiNR without kink (Fig. 3e). The signals are acquired by summing each column spectra of the three-dimensional dataset along the axial direction (perpendicular to the strain gradient) to enhance the signal-to-noise ratio (Methods). Figure 3f illustrates the vibrational spectra map for the transverse acoustic and transverse optical mode along the strain gradient direction. To better show the phonon spectra evolution under inhomogeneous strain, the EELS line profiles at each strain state are plotted in Fig. 3g. Similarly, as it moves from compressive to tensile strain under approximately 4.6% strain difference, the transverse acoustic mode exhibits a blueshift of approximately 1.5 meV, whereas the transverse optical mode exhibits a redshift of approximately 4.2 meV. This aligns well with the measured EELS profiles in Fig. 3b–d and the recorded results for transverse acoustic mode at a different location for the same straight SiNR (Extended Data Fig. 4). These STEM-EELS data, obtained at very high spatial and energy resolutions, provide direct evidence that phonon spectra could be significantly modified under an inhomogeneous strain field with a moderate strain gradient.

The as-acquired vibrational spectra encompass momentum-integrated vibrational modes across the entire Brillouin zone and closely resemble the projected phonon density of states[43]. In comparison with the experimental results, we performed ab initio calculations of the density of states and found good consistency for the phonon-mode evolution: as the elastic strain transitions from compression to tension, the transverse acoustic phonon exhibits a blueshift whereas the transverse optical phonon demonstrates a redshift, confirming the altered

vibrational states due to lattice distortion (Extended Data Fig. 5). This is also in good agreement with the theoretically calculated phonon dispersion under uniform strain[12,13]. Unlike previously observed EELS peak shift around heterointerface or defects, which are complicated by the coexistence of interfacial and/or defect phonon modes and strain gradient-modulated phonon modes[35,43], the observed peak shift in bent SiNRs is unequivocally attributed to lattice strain. This strain gradient-dependent shift in the phonon EELS spectra serves as a signature of phonon spectra broadening effect, which is responsible for the remarkable κ reduction, as discussed below in more detail.

Phonon spectra broadening effect

The statically distributed lattice strain induces a broadening effect in phonon frequency at a given wave vector, resulting in enhanced phonon scattering rates. For the simple case of a one-dimensional atomic chain with atomic mass of M, the phonon dispersion is given by $\omega = 2\sqrt{\frac{F}{M}} \sin\left(\frac{\pi}{2}\frac{\mathbf{k}}{\mathbf{k}_c}\right)$, where F and $\mathbf{k}$ are the force constant and phonon wave vector, respectively, and $\mathbf{k}_c$ is the cut-off wave vector[23,44,45]. This manifests as a single line for the relationship between ω and $\mathbf{k}$ that governs phonon transport through the atomic chain (Fig. 4a). However, for the case of bent SiNRs investigated in this work, the existence of a lattice strain gradient introduces external perturbations in atomic distances and, consequently, in effective interatomic force constants, F (Fig. 4a). This leads to a unique perturbation effect in phonon frequency (ω) and translates into the phonon spectra broadening effect evidenced by the EELS measurements (Fig. 3). Distinct from the case of uniform strain, where each phonon branch has a specific dispersion relation as a single line[12,13], the presence of inhomogeneous strain gives rise to a frequency distribution at a given wave vector (Fig. 4b, left).
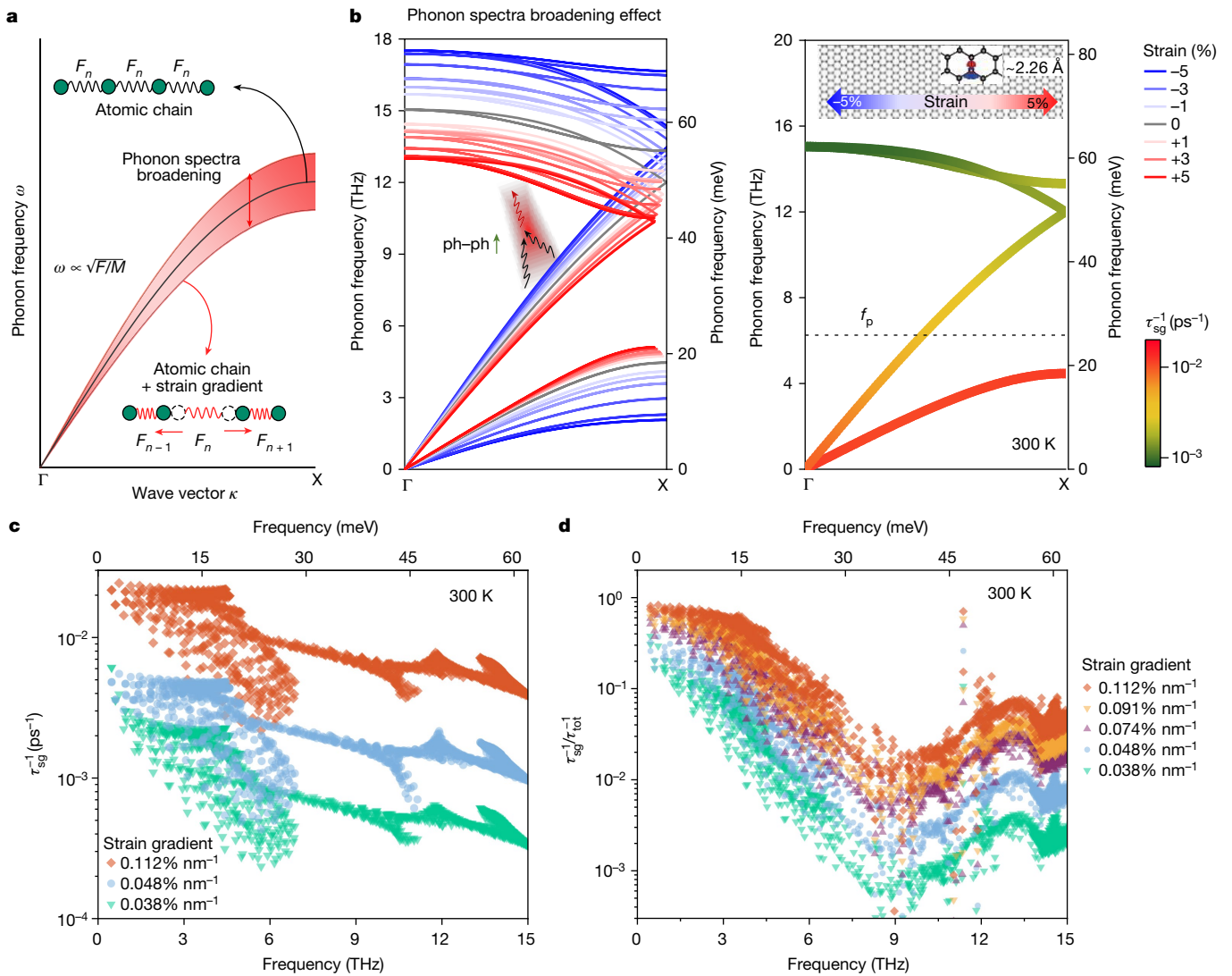
Fig. 4 | Modelling of inhomogeneous strain-induced phonon spectra broadening. a, Schematic illustration of the phonon dispersion modulation subjected to strain gradient. **b**, Left, calculated phonon dispersion of Si under different states of elastic strain. Right, strain-gradient-induced phonon scattering rate, τ_{sg}^{-1}, at 300 K of each phonon mode under strain gradient of 0.118% nm^{-1} (10% strain difference over 85 nm width). Right y axis represents the phonon frequency in meV. The characteristic phonon frequency at 300 K is

estimated as $f_p = k_B T/2\pi\hbar$, where k_B and $\hbar$ are the Boltzmann and reduced Planck constants, respectively. Inset, atomic interaction cut-off distance calculation using density functional theory. **c**, Phonon-mode-dependent scattering rate due to strain gradient, τ_{sg}^{-1}, under different strain gradients at 300 K. **d**, Ratio of strain gradient-induced phonon scattering over total phonon scattering rate, $\tau_{sg}^{-1}/\tau_{tot}^{-1}$, for each phonon mode at 300 K. Top x axis in (**c**) and (**d**) represent the phonon frequency in meV.

This phonon spectra broadening effect intensifies the diversity of available phonon frequencies, promoting faster relaxation of phonons back to their equilibrium states. Consequently, it accelerates phonon–phonon scattering rates and shortens the phonon lifetime. This presents as a fundamentally new phonon scattering mechanism that is absent in the context of uniform strain and is beyond conventional understanding.

To evaluate the impact of phonon spectra broadening on heat transport, we employed a combination of first-principles calculations and the Boltzmann transport equation[46,47] to model κ under varying magnitudes of inhomogeneous strain (Methods). To examine the influence of strain gradients on phonon transport, we calculated the atomic interaction cut-off distance[47], which reflects the phonon interaction radius in real space and thus determines how far a lattice vibration can sense the strain gradient (Methods). Based on this, we can calculate the strain gradient-induced phonon scattering rate, τ_{sg}^{-1}, which is shown for each phonon mode under the strain gradient of approximately 0.117% nm^{-1} (10% strain difference over 85 nm width) at 300 K (Fig. 4b,

right; Methods). We further compared our measured κ reduction of SiNRs under different bending strains with theoretical modelling. Indeed, the modelled κ demonstrated a larger reduction as the strain gradient increases, recapturing the trend of the experimentally measured results of bent SiNRs (Fig. 2b,h).

To further illustrate the altered phonon scattering process, we calculated phonon-mode-dependent scattering rates at 300 K with different strain gradient values. As the strain gradient increases, the phonon frequency distribution widens, which facilitates three-phonon scattering and results in an enlarged phonon scattering phase space (Supplementary Fig. 10). This is directly manifested by isolating the strain-gradient-induced phonon scattering term, τ_{sg}^{-1}, which increases by nearly one order of magnitude as the strain gradient increases from 0.038% nm^{-1} to 0.112% nm^{-1}. Furthermore, we evaluated the contribution of τ_{sg}^{-1} to the total phonon scattering rate τ_{tot}^{-1} through $\tau_{sg}^{-1}/\tau_{tot}^{-1}$ (Fig. 4d). It is evident that the strain gradient poses a more pronounced effect on heat-carrying acoustic phonons with frequencies below approximately 6 THz. This observation aligns well with the

Article

experimentally measured larger κ reduction as temperature reduces (Fig. 2b,h), as lower frequency acoustic phonons make a larger contribution to thermal transport at lower temperatures. The reduced contribution from low frequency phonons is further corroborated by the calculated κ accumulation curve (Supplementary Fig. 12). Taken together, as evidenced by the acquired EELS peak shift along the strain gradient, our theoretical modelling clearly verifies that the atomistic origin of this remarkable κ reduction in bent SiNRs indeed arises from the enhanced phonon scattering induced by the unique phonon spectra broadening effect.

Conclusions and outlook

Through developing experimental characterization tools that span from micrometre to atomic scale, and pairing with ab initio theoretical modelling, our study provides a crucial piece to the long-standing puzzle regarding the impact of inhomogeneous strain on phonon transport. As a result, this study not only unequivocally reveals the remarkable impact of inhomogeneous strain on thermal transport, but also offers insights for the innovative design of strain-engineering-enabled functional devices. For example, the synergistic interplay between the reduction in lattice κ induced by strain gradients and the previously demonstrated enhancement of carrier mobility[27,48] presents a new strategy for developing high-performance thermoelectric energy converters. Additionally, this degree of κ modulation can enable functional thermal switches through elastically tuning inhomogeneous strain in nanoribbon arrays for dynamic heat flux control.

Online content

Any methods, additional references, Nature Portfolio reporting summaries, source data, extended data, supplementary information, acknowledgements, peer review information; details of author contributions and competing interests; and statements of data and code availability are available at https://doi.org/10.1038/s41586-024-07390-4.

1. Balaghi, L. et al. Widely tunable GaAs bandgap via strain engineering in core/shell nanowires with large lattice mismatch. *Nat. Commun.* **10**, 2793 (2019).
2. Conesa-Boj, S. et al. Boosting hole mobility in coherently strained [110]-oriented Ge–Si core–shell nanowires. *Nano Lett.* **17**, 2259–2264 (2017).
3. Zhu, C. et al. Strain engineering in perovskite solar cells and its impacts on carrier dynamics. *Nat. Commun.* **10**, 815 (2019).
4. Jiang, J. et al. Synergistic strain engineering of perovskite single crystals for highly stable and sensitive X-ray detectors with low-bias imaging and monitoring. *Nat. Photonics* **16**, 575–581 (2022).
5. Jiang, M. et al. Strain-regulated Gibbs free energy enables reversible redox chemistry of chalcogenides for sodium ion batteries. *Nat. Commun.* **13**, 5588 (2022).
6. Li, J., Shan, Z. & Ma, E. Elastic strain engineering for unprecedented materials properties. *MRS Bull.* **39**, 108–114 (2014).
7. Choi, E.-M. et al. 3D strain-induced superconductivity in La₂CuO₄₊δ using a simple vertically aligned nanocomposite approach. *Sci. Adv.* **5**, eaav5532 (2019).
8. Ling, T. et al. Activating cobalt(II) oxide nanorods for efficient electrocatalysis by strain engineering. *Nat. Commun.* **8**, 1509 (2017).
9. Wu, G. et al. In-plane strain engineering in ultrathin noble metal nanosheets boosts the intrinsic electrocatalytic hydrogen evolution activity. *Nat. Commun.* **13**, 4200 (2022).
10. Zhou, Y., Dong, Z. Y., Hsieh, W. P., Goncharov, A. F. & Chen, X. J. Thermal conductivity of materials under pressure. *Nat. Rev. Phys.* **4**, 319–335 (2022).
11. Li, S. et al. Anomalous thermal transport under high pressure in boron arsenide. *Nature* **612**, 459–464 (2022).
12. Li, X., Maute, K., Dunn, M. & Yang, R. Strain effects on the thermal conductivity of nanostructures. *Phys. Rev. B* **81**, 245318 (2010).
13. Parrish, K. D., Jain, A., Larkin, J. M., Saidi, W. A. & McGaughey, A. J. H. Origins of thermal conductivity changes in strained crystals. *Phys. Rev. B* **90**, 235201 (2014).
14. Hohensee, G. T., Fellinger, M. R., Trinkle, D. R. & Cahill, D. G. Thermal transport across high-pressure semiconductor-metal transition in Si and Si₀.₉₉₁Ge₀.₀₀₉. *Phys. Rev. B* **91**, 205104 (2015).
15. Murphy, K. F., Piccione, B., Zanjani, M. B., Lukes, J. R. & Gianola, D. S. Strain- and defect-mediated thermal conductivity in silicon nanowires. *Nano Lett.* **14**, 3785–3792 (2014).
16. Lee, S. M., Cahill, D. G. & Venkatasubramanian, R. Thermal conductivity of Si–Ge superlattices. *Appl. Phys. Lett.* **70**, 2957 (1998).
17. Abramson, A. R., Tien, C. L. & Majumdar, A. Interface and strain effects on the thermal conductivity of heterostructures: A molecular dynamics study. *J. Heat Transfer* **124**, 963–970 (2002).
18. Hopkins, P. E. et al. Effects of coherent ferroelastic domain walls on the thermal conductivity and Kapitza conductance in bismuth ferrite. *Appl. Phys. Lett.* **102**, 121903 (2013).
19. Sarantopoulos, A., Ong, W.-L., Malen, J. A. & Rivadulla, F. Effect of epitaxial strain and vacancies on the ferroelectric-like response of CaTiO₃ thin films. *Appl. Phys. Lett.* **113**, 182902 (2018).
20. Ning, S. et al. Anomalous defect dependence of thermal conductivity in epitaxial WO₃ thin films. *Adv. Mater.* **31**, 1903738 (2019).
21. Carruthers, P. Theory of thermal conductivity of solids at low temperatures. *Rev. Mod. Phys.* **33**, 92 (1961).
22. Herring, C. Role of low-energy phonons in thermal conduction. *Phys. Rev.* **95**, 954 (1954).
23. Klemens, P. G. The scattering of low-frequency lattice waves by static imperfections. *Proc. Phys. Soc. A* **68**, 1113–1128 (1955).
24. Dai, Z., Liu, L. & Zhang, Z. Strain engineering of 2D materials: issues and opportunities at the interface. *Adv. Mater.* **31**, 1805417 (2019).
25. Moore, A. L. & Shi, L. Emerging challenges and materials for thermal management of electronics. *Mater. Today* **17**, 163–174 (2014).
26. Pop, E. Energy dissipation and transport in nanoscale devices. *Nano Res.* **3**, 147–169 (2010).
27. Chu, M., Sun, Y., Aghoram, U. & Thompson, S. E. Strain: a solution for higher carrier mobility in nanoscale MOSFETs. *Annu. Rev. Mater. Res.* **39**, 203–229 (2009).
28. Gu, X., Li, X. & Yang, R. Phonon transmission across Mg₂Si/Mg₂Si₁₋ₓSnₓ interfaces: a first-principles-based atomistic Green's function study. *Phys. Rev. B* **91**, 205313 (2015).
29. Capinski, W. S. & Maris, H. J. Thermal conductivity of GaAs/AlAs superlattices. *Physica B Condens. Matter* **219–220**, 699–701 (1996).
30. Li, H. et al. Optoelectronic crystal of artificial atoms in strain-textured molybdenum disulfide. *Nat. Commun.* **6**, 7381 (2015).
31. Krivanek, O. L. et al. Vibrational spectroscopy in the electron microscope. *Nature* **514**, 209–212 (2014).
32. Venkatraman, K., Levin, B. D. A., March, K., Rez, P. & Crozier, P. A. Vibrational spectroscopy at atomic resolution with electron impact scattering. *Nat. Phys.* **15**, 1237–1241 (2019).
33. Haas, B. et al. Atomic-resolution mapping of localized phonon modes at grain boundaries. *Nano Lett.* **23**, 5975–5980 (2023).
34. Qi, R. et al. Four-dimensional vibrational spectroscopy for nanoscale mapping of phonon dispersion in BN nanotubes. *Nat. Commun.* **12**, 1179 (2021).
35. Qi, R. et al. Measuring phonon dispersion at an interface. *Nature* **599**, 399–403 (2021).
36. Yang, L. et al. Thermal conductivity of individual silicon nanoribbons. *Nanoscale* **8**, 17895–17901 (2016).
37. Yang, L. et al. Kink as a new degree of freedom to tune the thermal conductivity of Si nanoribbons. *J. Appl. Phys.* **126**, 155103 (2019).
38. Shi, L. et al. Measuring thermal and thermoelectric properties of one-dimensional nanostructures using a microfabricated device. *J. Heat Transfer* **125**, 881–888 (2003).
39. Yang, L. et al. Observation of superdiffusive phonon transport in aligned atomic chains. *Nat. Nanotechnol.* **16**, 764–768 (2021).
40. Yang, L. et al. High thermoelectric figure of merit of porous Si nanowires from 300 to 700 K. *Nat. Commun.* **12**, 3926 (2021).
41. Liu, L.-C., Huang, M.-J., Yang, R., Jeng, M.-S. & Yang, C.-C. Curvature effect on the phonon thermal conductivity of dielectric nanowires. *J. Appl. Phys.* **105**, 104313 (2009).
42. Gao, P. et al. Atomic-scale measurement of flexoelectric polarization at SrTiO₃ dislocations. *Phys. Rev. Lett.* **120**, 267601 (2018).
43. Yan, X. et al. Single-defect phonons imaged by electron microscopy. *Nature* **589**, 65–69 (2021).
44. Wu, Y. et al. Lattice strain advances thermoelectrics. *Joule* **3**, 1276–1288 (2019).
45. Wu, Y. et al. Thermoelectric enhancements in PbTe alloys due to dislocation-induced strains and converged bands. *Adv. Sci.* **7**, 1902608 (2020).
46. Kresse, G. & Joubert, D. From ultrasoft pseudopotentials to the projector augmented-wave method. *Phys. Rev. B* **59**, 1758–1775 (1999).
47. Li, W., Carrete, J., Katcho, N. A. & Mingo, N. ShengBTE: a solver of the Boltzmann transport equation for phonons. *Comput. Phys. Commun.* **185**, 1747–1758 (2014).
48. Niquet, Y.-M., Delerue, C. & Krzeminski, C. Effects of strain on the carrier mobility in silicon nanowires. *Nano Lett.* **12**, 3545–3550 (2012).

Methods

Si nanoribbon fabrication

The SiNRs were fabricated from 6 inch (150 mm) silicon-on-insulator (SOI) wafers (p-type boron doped Si <100> with a dopant concentration of 0.7–1.5 × 10¹⁵ cm⁻³, SimguiTechnology Co., Ltd). The SOI wafers possess a 140-nm-thick top silicon device layer and a 500 nm buried oxide layer. In the fabrication process, the SOI wafer first went through a thermal oxidation process to oxidize a targeted thickness of the device silicon layer, after which the resulted silicon oxide layer was removed with buffered oxide etch (6:1). Then the wafer was cut into 30 mm × 30 mm pieces and patterned into nanoribbons using E-beam lithography (JEOL 6300) and reactive ion plasma etching (Oxford PlasmaPro), leading to ribbons anchored on two separated islands (Supplementary Fig. 1). Note that during E-beam lithography, to compensate for the interference effects between the electron beams, proximity effect correction was performed using NanoPECS software. Finally, wet hydrofluoric acid etching (10:1) and critical point dry were used to remove the underneath oxide and release the Si nanoribbons into freestanding structures.

Si nanoribbon bending procedures

To introduce strain gradient within the ribbon, one end of the ribbon is first picked up by a sharp tungsten microprobe with tip radius of approximately 100 nm, with the other end well attached with the flat Pt electrode via van der Waals interaction (Extended Data Fig. 6). Then, through careful manipulation using the microprobe, we deliberately bend the nanoribbon with certain curvature, as shown in Fig. 1d,e. After this, both ends of the sample are firmly anchored with the underlying Pt electrodes via electron-beam-induced deposition of Pt/C. By doing this, we are able to exclusively introduce an inhomogeneous strain field within the nanoribbon without the complexity of involving other factors, such as interfaces, defects, etc. A visual representation of the entire sample preparation process is also provided in an accompanying illustration video (Supplementary video 1). The elastic strain distribution is numerically calculated based on the geometry and bending configuration using finite element modelling.

κ measurement

We conducted the κ measurements in a cryostat (Janis CCS-400/204) operated under a high vacuum (<1 × 10⁻⁶ mbar) with a dual radiation shield configuration. For κ measurements, a Wheatstone bridge scheme was applied at the sensing side to improve measurement sensitivity (approximately 36 pW K⁻¹). The background thermal conductance between the suspended membranes was measured separately and subtracted from the measured thermal conductance of the sample. To evaluate the κ, we obtained the cross-sectional area of tested samples by measuring the width using SEM and thickness using atomic force microscopy. We have confirmed that the contact thermal resistance poses negligible effects on the measured total thermal resistance (Extended Data Fig. 7), and the detailed examination on the effects of contact thermal resistance can be found in Supplementary Note 3.

Strain distribution analysis

The initial geometric model of each SiNR sample is constructed in a commercial finite element software, ABAQUS, exactly following its dimensions measured in experiments. We used beam elements considering the geometric nonlinearity with mesh sensitivity verified. The bent SiNRs with different configurations are simulated by the loads applied only at the two ends, aligning with the actual experimental setting. Note that for straight SiNRs, a small perturbation load (in addition to the end loads) is first used to initiate instability and then released after the desired configuration is achieved. We identified the maximum principal strain ε_{max} in the deformed configuration of each

ribbon. We calculated the arclength of the ribbon whose cross-section is subject to principal strain greater than $0.5\varepsilon_{max}$. The ratio of this calculated arclength to the total length of the ribbon is roughly the same within each group of bent SiNRs without and with kink. Specifically, the ratio is 57.5% and 54.9% for the bent SiNR nos. 1 and 2 and is 36.4%, 32.2%, 38.9% and 35.5% for bent SiNR with kink nos. 1, 2, 3 and 4, respectively.

EELS characterization

The EELS data was acquired on a Nion U-HERMES200 microscope equipped with both a monochromator and aberration corrector, with an approximately 10 pA beam current operated at 60 kV. Although such a measurement can reach atomic resolutions for Si (refs. 32,33), the resolution here was set to be sub-nanometre scale to precisely correlate with the nanoscale strain distribution and further avoid the possible complicating effects between the on-column and off-column measurements[32,33]. The point analysis spectra are acquired at the five selected points along the strain gradient (Fig. 3b,c). An electron beam with a convergence semi-angle of 20 mrad was used, and the collection semi-angle of the circular aperture with diameter of 1 mm is 25 mrad. The point analysis spectra are averaged using long acquisition time and measuring about 50 times to reduce the signal noise. The three-dimensional EELS datasets were acquired with 35 mrad convergence semi-angle and 25 mrad collection semi-angle. The typical energy resolution under these conditions is about 8.5 meV, and the spatial resolution is better than 220 pm. The typical dwell time was 2–5 s per pixel and approximately 120 min for each dataset in total (30 pixel × 50 pixel, but slightly adjusted for each dataset). The acquired spectra of the three-dimensional EELS datasets were first aligned by the zero-loss peak position to correct possible beam energy drift. After the alignment, the spectra were normalized by the zero-loss peak total intensity. Then the block-matching and three-dimensional filtering (BM3D) algorithm was applied to remove Gaussian noise[49]. After that, the zero-loss peak was removed by fitting the spectra to the Pearson VII function[50] with two energy windows, 13–18 meV and 200–230 meV (one before and one after the energy-loss region). Lucy–Richardson deconvolution was then employed to ameliorate the broadening effect caused by the finite energy resolution[35,51], taking the zero-loss peak as the point spread function, where the zero-loss peak is acquired in vacuum containing no phonon signals. Finally, the spectra were summed along the axial direction (perpendicular to the strain gradient direction) to enhance the signal-to-noise ratio. The Gaussian fits of the EELS peaks give the energy of the peaks.

Modelling phonon transport under inhomogeneous strain

To investigate the phonon spectra broadening effect, we compared the modelled reduction in κ for bulk Si with and without strain gradient to the experimentally measured κ reduction of the SiNRs (Fig. 2). We performed density functional theory simulations through the finite displacement method to obtain phonon dispersions under different elastic strain states (Fig. 4b, left). The inhomogeneous strain drives a significant phonon frequency shift in the whole Brillouin zone of bent SiNRs, resulting in a broadened phonon spectrum. The phonon spectra broadening effect can induce an additional scattering process for phonons subjected to inhomogeneous strain. Under the framework of Matthiessen's rule, the total phonon scattering rates, τ_{tot}^{-1}, considering the effects of inhomogeneous strain, can be expressed as

$$\frac{1}{\tau_{tot}} = \frac{1}{\tau_{BTE}} + \frac{1}{\tau_{sg}}, \tag{1}$$

where τ_{BTE}^{-1} is the original phonon scattering rate of bulk Si from Sheng-BTE calculations[47], and the phonon scattering rate induced by inhomogeneous strain is given by

Article

$$\frac{1}{\tau_{\mathrm{sg}}} = \alpha \times f \times \Delta\Omega. \qquad (2)$$

Here f is the Bose–Einstein distribution, $\Delta\Omega$ is total phonon frequency shift under the given inhomogeneous strain field, and α is the ratio of the atomic interaction cutoff distance to the size of the inhomogeneous strain field. To determine how far the lattice vibration could sense the strain gradient, we calculated the atomic interaction cut-off distance (r_c) in Si (ref. 47), which reflects the phonon interaction radius in real space. Assuming the broadened phonon spectra to be linearly distributed in real space (Extended Data Fig. 8), we then calculate the ratio of r_c over the nanoribbon width W_{SiNR} as $\alpha = \frac{r_\mathrm{c}}{W_{\mathrm{SiNR}}}$, and $\alpha \times \Delta\Omega$ represents the actual phonon frequency perturbation under given elastic strain gradient (Fig. 4b, left). Based on Fermi's golden rules, $\Delta\Omega$ is given by the transition rate from phonon mode $\mathbf{q}j$ to phonon mode $\mathbf{q}'j'$ under the perturbations of inhomogeneous strain in Si, which can be written as[52–59]

$$\Delta\Omega = \sum_{\mathbf{q}'j'} \frac{\pi V}{\omega v_\mathrm{g}} \, |\langle \mathbf{q}'j' | T(\omega) | \mathbf{q}j \rangle|^2 \, \delta(\omega_{\mathbf{q}'j'} - \omega_{\mathbf{q}j}). \qquad (3)$$

Here V is the unit cell volume, $|\mathbf{q}j\rangle$ is the phonon eigenstate, $\mathbf{q}$ and j denote the wave vector and phonon polarization, respectively, v_g is the phonon group velocity of phonon mode $\mathbf{q}j$, and ω is the phonon frequency. Here, $\delta(\mathrm{x}) = +\infty$ when $\mathrm{x} = 0$, $\delta(\mathrm{x}) = 0$ when $\mathrm{x} \neq 0$, and $\int_{-\infty}^{+\infty} \delta(\mathrm{x})\mathrm{dx} = 1$. Note that equation (3) describes an energy-conserved scattering process between the annihilated phonon with mode $\mathbf{q}j$ and created phonon with mode $\mathbf{q}'j'$, while the Bose–Einstein distribution f in equation (3) tallies the scattering events through taking into account the overall quantity of created phonons. $T(\omega)$ represents the transfer matrix element between $|\mathbf{q}j\rangle$ and $|\mathbf{q}'j'\rangle$. For weak perturbations, the transfer matrix T can be simplified using the Born approximation[59,60]

$$T = H_{\mathrm{sg}} \sum_{n=0} (G_0 H_{\mathrm{sg}})^n \approx H_{\mathrm{sg}}, \qquad (4)$$

where H_{sg} is the perturbation Hamiltonian[59,60], and G_0 is the retarded Green's function of the unperturbed crystal. The perturbation Hamiltonian in the matrix form can be expressed as $H_{\mathrm{sg}} = \frac{\Phi_{\mathrm{sg}} - \Phi_0}{M_{\mathrm{Si}}}$, where M_{Si} is the atomic mass of silicon, Φ_{sg} and Φ_0 represent the effective harmonic interatomic force constants for the strain gradient-modulated and unperturbed crystal, respectively.

All the simulations were conducted using the density functional theory method and implemented in the Vienna ab initio simulation package[61,62]. The projector augmented wave method[46,63] and generalized gradient approximation with the Perdew–Burke–Ernzerhof exchange-correlation functional were adopted[64]. The plane-wave cut-off was set to 500 eV and the energy criterion for self-consistent convergence was 1×10^{-6} eV. A $4 \times 4 \times 4$ Monkhorst–Pack k-mesh, including the Γ point, was used to sample the whole Brillouin zone. The Hellmann–Feynman forces tolerance value was taken as 1×10^{-7} eV Å^{-1} for all geometric optimizations. The convergence of the kinetic energy cut-off and k-mesh were examined.

Data availability

Codes central to the main work described in this manuscript are deposited in Code Ocean (https://codeocean.com/capsule/9335891/tree). Source data are provided with this paper.

49. Dabov, K., Foi, A., Katkovnik, V. & Egiazarian, K. Image denoising by sparse 3-D transform-domain collaborative filtering. *IEEE Trans. Image Process.* **16**, 2080–2095 (2007).
50. Hall, M. M. Jr, Veeraraghavan, V. G., Rubin, H. & Winchell, P. G. The approximation of symmetric X-ray peaks by Pearson type VII distributions. *J. Appl. Cryst.* **10**, 66–68 (1977).
51. Bellido, E. P., Rossouw, D. & Botton, G. A. Toward 10 meV electron energy-loss spectroscopy resolution for plasmonics. *Microsc. Microanal.* **20**, 767–778 (2014).
52. Mingo, N., Esfarjani, K., Broido, D. A. & Stewart, D. A. Cluster scattering effects on phonon conduction in graphene. *Phys. Rev. B* **81**, 045408 (2010).
53. Kundu, A., Mingo, N., Broido, D. A. & Stewart, D. A. Role of light and heavy embedded nanoparticles on the thermal conductivity of SiGe alloys. *Phys. Rev. B* **84**, 125426 (2011).
54. Stern, R., Wang, T., Carrete, J., Mingo, N. & Madsen, G. K. H. Influence of point defects on the thermal conductivity of FeSi. *Phys. Rev. B* **97**, 195201 (2018).
55. Katre, A., Carrete, J., Wang, T., Madsen, G. K. H. & Mingo, N. Phonon transport unveils the prevalent point defects in GaN. *Phys. Rev. Mater.* **2**, 050602(R) (2018).
56. Polanco, C. A. & Lindsay, L. Thermal conductivity of InN with point defects from first-principles. *Phys. Rev. B* **98**, 014306 (2018).
57. Polanco, C. A. & Lindsay, L. Ab initio phonon point defect scattering and thermal transport in graphene. *Phys. Rev. B* **97**, 014303 (2018).
58. Protik, N. H., Carrete, J., Katcho, N. A., Mingo, N. & Broido, D. Ab initio study of the effect of vacancies on the thermal conductivity of boron arsenide. *Phys. Rev. B* **94**, 045207 (2016).
59. Guo, R. & Lee, S. Mie scattering of phonons by point defects in IV–VI semiconductors PbTe and GeTe. *Mater. Today Phys.* **12**, 100177 (2020).
60. Economou, E. N. *Green's Functions in Quantum Physics*, Vol. 7 (Springer, 2006).
61. Kresse, G. & Furthmüller, J. Efficient iterative schemes for ab initio total-energy calculations using a plane-wave basis set. *Phys. Rev. B* **54**, 11169–11186 (1996).
62. Kresse, G. & Furthmüller, J. Efficiency of ab-initio total energy calculations for metals and semiconductors using a plane-wave basis set. *Comput. Mater. Sci.* **6**, 15–50 (1996).
63. Blöchl, P. E. Projector augmented-wave method. *Phys. Rev. B* **50**, 17953–17979 (1994).
64. Perdew, J. P., Burke, K. & Ernzerhof, M. Generalized gradient approximation made simple. *Phys. Rev. Lett.* **77**, 3865–3868 (1996).

Author contributions L.Y. proposed and directed the research. L.Y. fabricated the Si nanoribbons and performed thermal conductivity measurements while working in D.L.'s lab. J.D. performed EELS measurements and analysis, electron diffraction, and GPA analysis under the direction of P.G. S.Q. carried out the preparation of TEM samples and helped with data processing. H.L. and Z.D. conducted strain distribution analyses. S.Y., Y.T. and L.Y. performed theoretical modelling. The manuscript was prepared and revised by L.Y., J.D., S.Y., D.L. and P.G. with input from all co-authors.
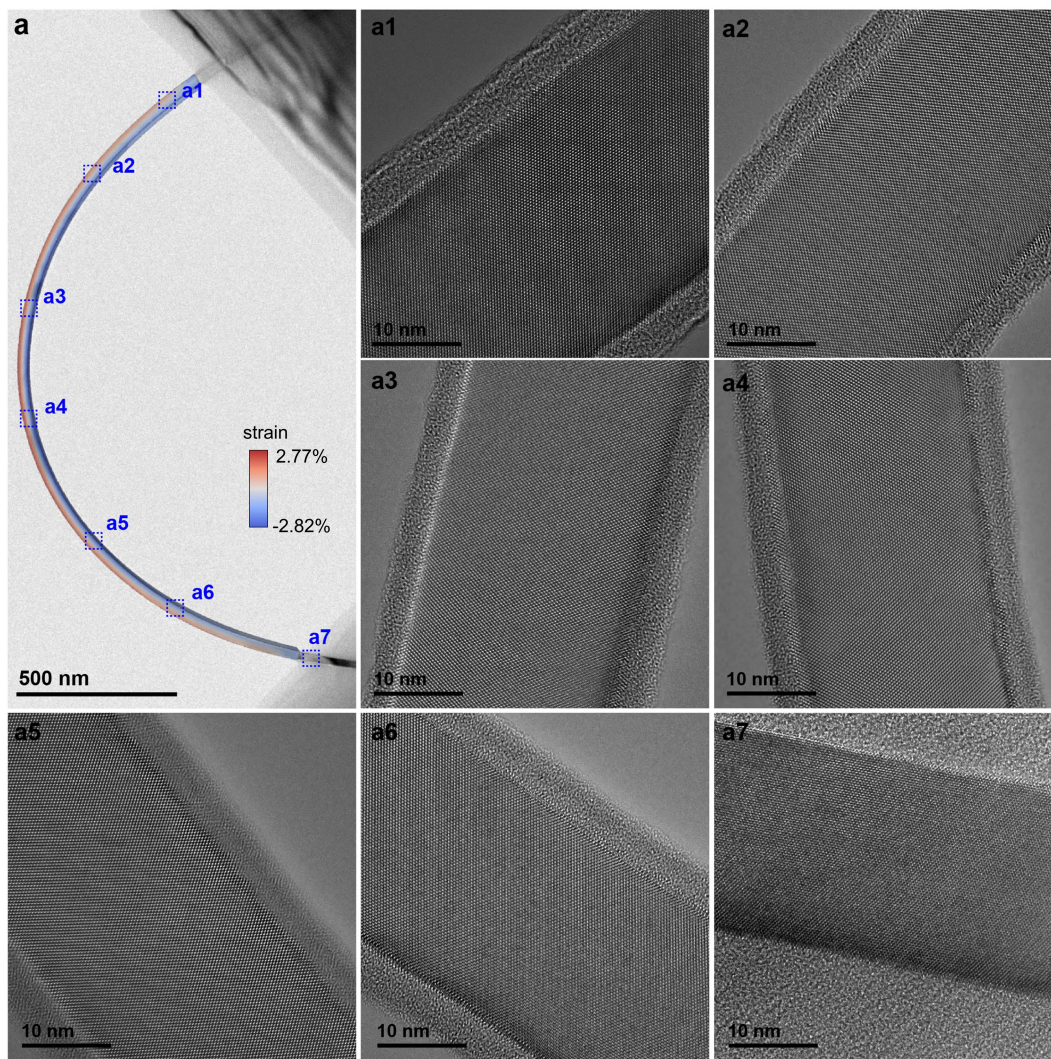
Extended Data Fig. 1 | HRTEM examination showing the single crystalline nature of the bent SiNR. (a) TEM image of a bent SiNR. (a1-a7) HRTEM images covering the full width of the examined region for the bent SiNR in (a), and the blue dashed rectangles in (a) mark the different locations along the length of the bent SiNR for HRTEM tests.
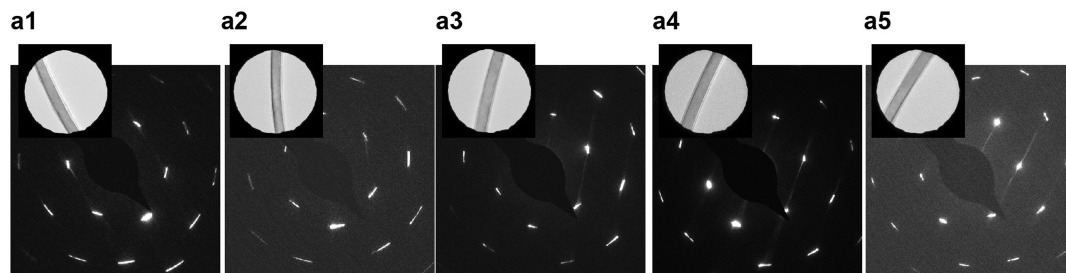
Extended Data Fig. 2 | SAED patterns of a bent SiNR. (a1-a5) SAED patterns of the bent SiNR, where the inserts show the corresponding portion of the sample in Extended Data Fig. 1 within the selected aperture with diameter of ~180 nm.
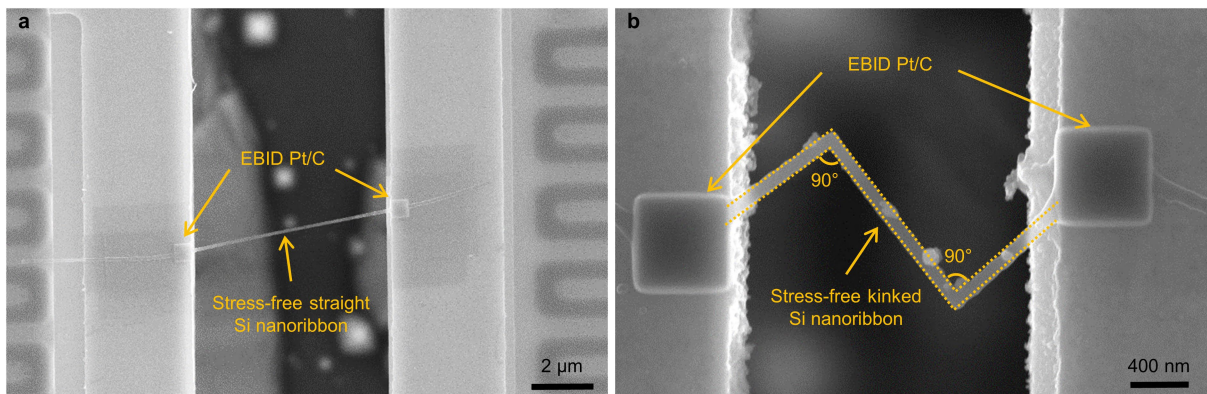
Extended Data Fig. 3 | Stress-free sample. (a) SEM image of the stress-free straight Si nanoribbon sample, where the ends are treated with EBID Pt/C composite to minimize the effects of contact thermal resistance. (b) SEM image of the stress-free kinked Si nanoribbon sample. Note that the kinked Si nanoribbon are patterned with 90° kink angle, and thus the straight dashed line delineating on the ribbon edge as well as 90° kink angle formed between the two kink arms suggest this kinked ribbon is in stress-free condition.
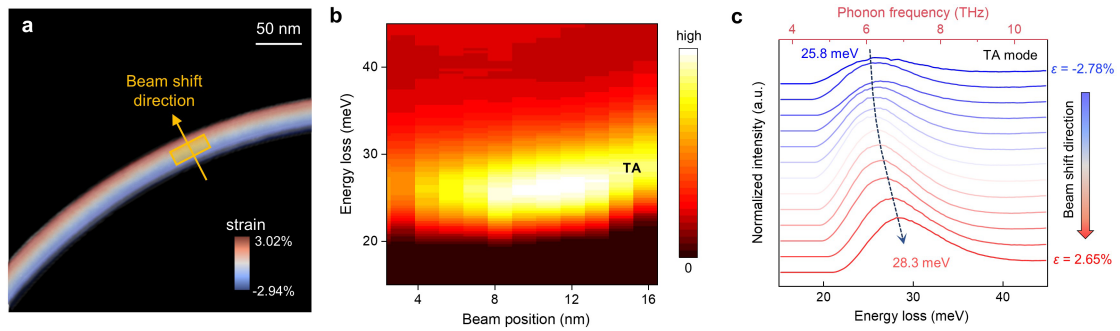
Extended Data Fig. 4 | Measured EELS map of the transverse acoustic mode under bending. (a) HAADF image for the bent Si nanoribbon without kink, and the calculated strain contour is overlaid on top to visualize the strain distribution. The yellow rectangle represents the area where the EELS signals are acquired by summing each column spectra of the three-dimension dataset along the axial direction (perpendicular to the strain gradient direction) to enhance the signal-to-noise ratio. (b) The vibrational spectra map for the transverse acoustic (TA) mode along the beam shift direction. (c) Measured EELS profiles for the TA phonon mode along the strain gradient, which shows a peak shift from 25.8 meV to 28.3 meV as the strain changes from -2.78% to 2.65%.
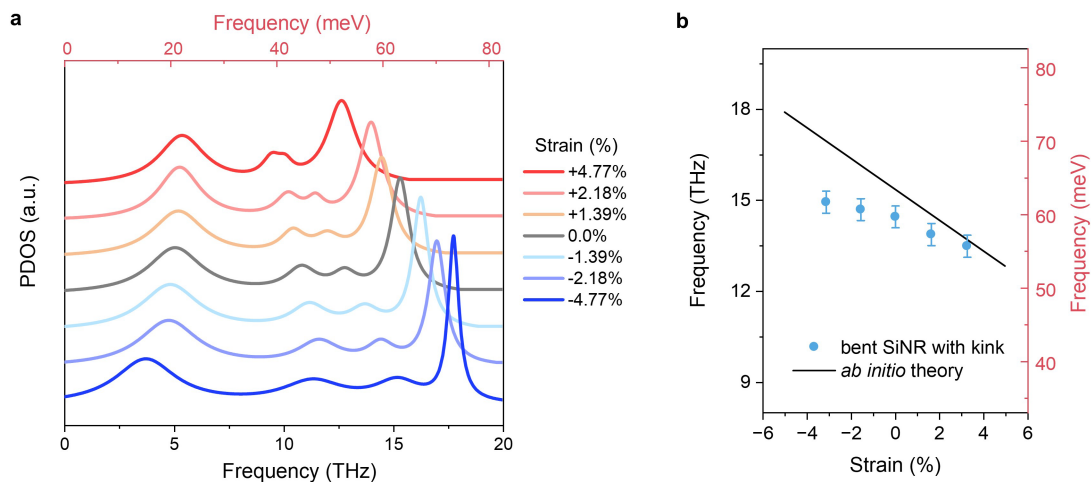
Extended Data Fig. 5 | Calculated phonon density of states under elastic strain. (a) Calculated phonon density of states (PDOS) of Si atoms as the elastic strain changes from 4.77% to −4.77%. (b) Extracted TO peak position for the measured bent SiNR with kink in Fig. 3b–d as a function of elastic strain, where the theoretically calculated peak position for the TO mode is also plotted for comparison. Error bars represent the peak fitting error. Note that the slight discrepancy between the experimental results and theoretical calculation could be caused by local uniform strain approximations in DFT to reproduce the inhomogeneous strain distribution in bent Si nanoribbons, and measurement uncertainties in EELS due to the limited energy resolutions, as well as errors introduced during background subtraction and phonon peak fitting.
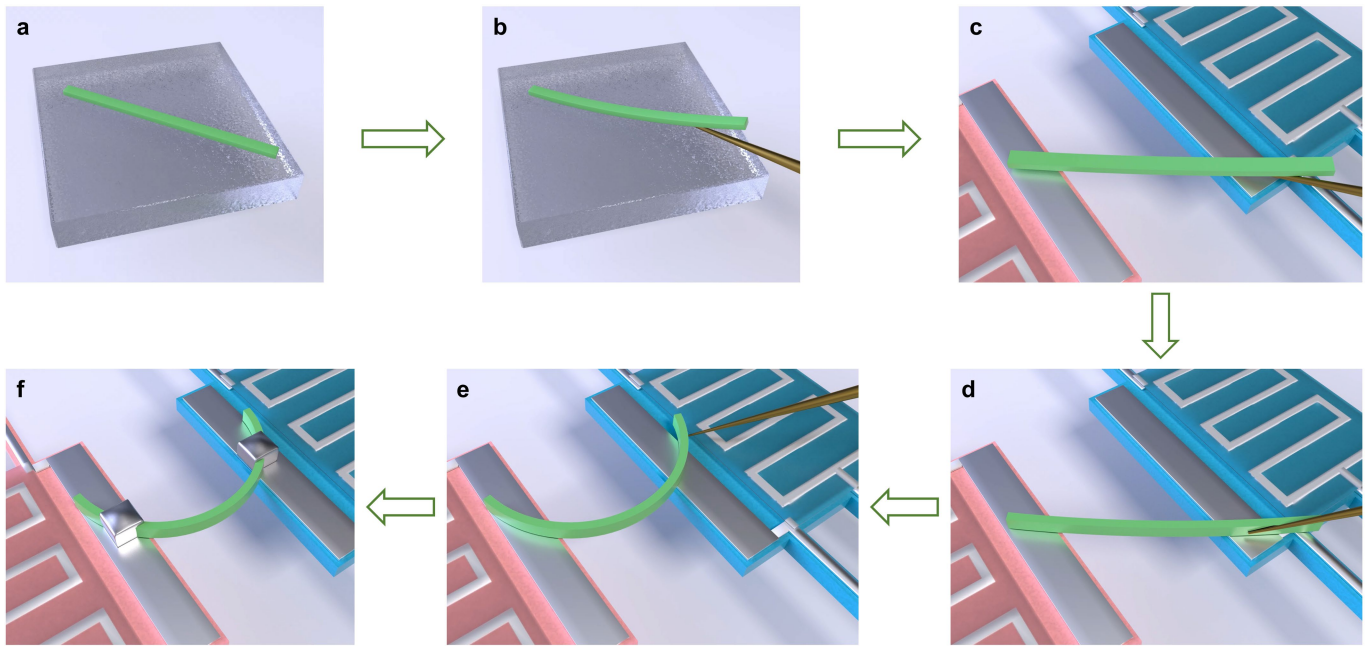
Extended Data Fig. 6 | Bent Si nanoribbon sample preparation procedures.
(a-b) A Si nanoribbon initially rested on a PDMS substrate and was picked up by a microprobe through van der Waals interaction. (c) The ribbon sample was placed on the suspended microdevice to bridge the gap of the two suspended membranes. (d) The nanoribbon was inverted to present its thickness side upward using the microprobe. (e) One end of the ribbon adhered well with the underlying electrode via van der Waals interaction, and the other end was moved by the microprobe to achieve the desired bending configuration. (f) The two ends of the bent ribbon were fixed with the underlying electrode through focused electron beam induced deposition (EBID) of Pt/C composite.
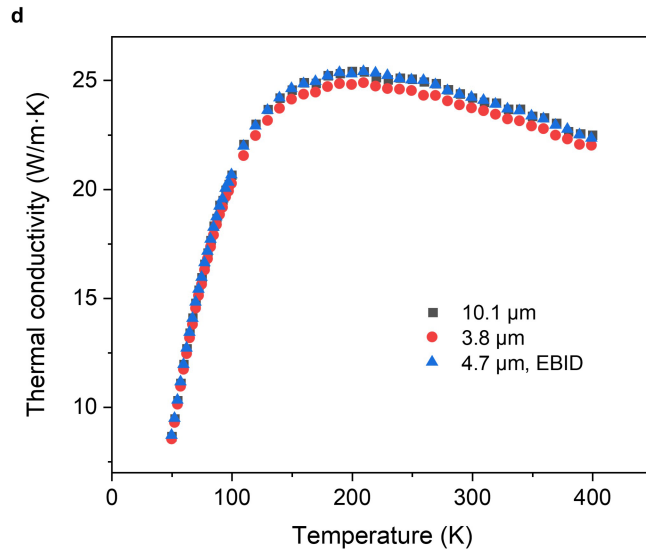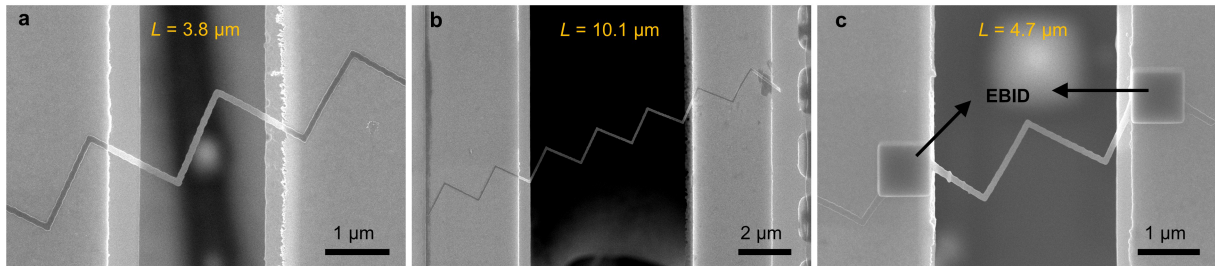
Extended Data Fig. 7 | Contact thermal resistance characterization. SEM images of the 34 nm thick, 85 nm wide kinked SiNR with suspended length, L, of (a) 3.8 μm, and (b) 10.1 μm, respectively. (c) SEM image of the (34, 85) kinked SiNR with suspended length of 4.7 μm. The electron beam induced deposition (EBID) of Pt/C composite is performed at the two ends. (d) Measured thermal conductivity of the three samples in (a-c) in the temperature range from 50–400 K, where the close thermal conductivity indicates the negligible contribution from the contact thermal resistance.

a

b
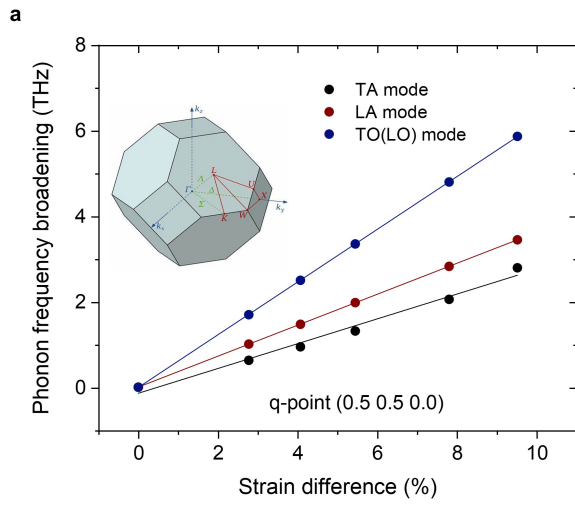
Extended Data Fig. 8 | Phonon frequency broadening as a function of elastic strain difference. Calculated absolute value of phonon frequency broadening for TA, LA, and TO (LO) modes as a function of strain difference at the selected q-points of (a) (0.5, 0.5, 0.0) and (b) (0.75, 0.5, 0.25), respectively.
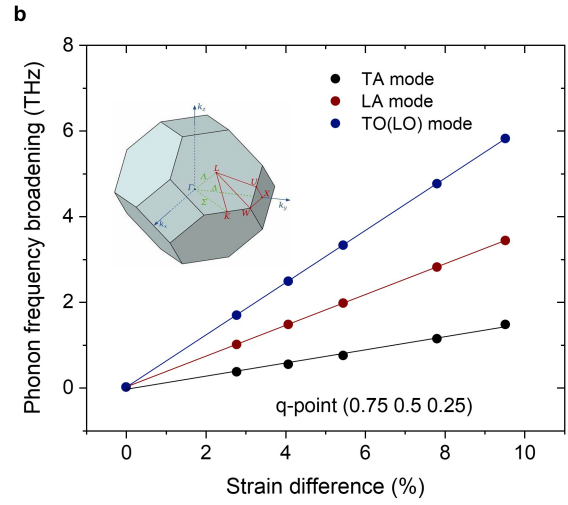
As the elastic strain is linearly distributed along the thickness direction for a bent Si nanoribbon (Supplementary Fig. 3), and the phonon frequency shift is linearly dependent on elastic strain, this in turn validates our assumption that the broadened phonon spectra are linearly distributed in real space.